P7.4 SIMULATED WSR-88D MEASUREMENTS OF A TORNADO HAVING A WEAK REFLECTIVITY CENTER

Vincent T. Wood[1], David C. Dowell[2], and Rodger A. Brown[1]
[1]NOAA, National Severe Storms Laboratory
[2]Cooperative Institute for Mesoscale Meteorological Studies,
University of Oklahoma, Norman, Oklahoma

1. INTRODUCTION

Our previous conceptual studies compared WSR-88D measurements in tornadoes with simulated data based on Rankine (1901) combined vortex (e.g., Brown 1998; Brown and Lemon 1976; Brown et al. 1978, Brown et al. 2002; Wood and Brown 1997). For these simulations, it was assumed that reflectivity was uniform across the vortex.

How the horizontal profile of reflectivity across the vortex varied with height and stage of tornado evolution was not well understood until proximity radar observations of tornadoes revealed details about the three-dimensional structures of tornado vortex and concentric and spiral bands of reflectivity surrounding a low-reflectivity eye of the vortex (Bluestein and Pazmany 2000; Wurman and Gill 2000; Wurman 2002). Aloft, a reflectivity minimum occurs inside the tornado core with a high-reflectivity annulus being slightly wider than the tornado's core radius at which maximum tangential velocity occurs. The annulus tapers towards the ground. The minimum in reflectivity within the tornado core implies the centrifuging of radar scatterers by the vortex (Snow 1984; Wakimoto and Martner 1992; Bluestein and Pazmany 2000; Dowell et al. 2004).

Dowell et al. (2004) show that radar scatterer motion and airflow within the tornado are different. Relatively dense objects move outward relative to the airflow and move slower in the tangential direction. Additionally, the maximum in tangential object motion occurs beyond the tornado's core radius at which the peak tangential velocity of the airflow occurs. Centrifuging of hydrometeors and debris rapidly produces a minimum in number concentration within the vortex core and a maximum in a surrounding annulus. The degree of accumulation of precipitation particles in the annulus, and the rate of expansion of the annulus, increase with precipitation particle sizes.

The purpose of this paper is to investigate how the high-reflectivity annulus surrounding the low-reflectivity eye of the tornado vortex can affect simulated WSR-88D Doppler velocity measurements across the vortex. Following the approach of Dowell et al. (2004), a numerical tornado model was used to simulate the characteristics of a tornado. The model used important processes that included centrifugal effects on precipitation particles by the swirling flow.

Corresponding author address: Vincent T. Wood, National Severe Storms Laboratory, 1313 Halley Circle, Norman, OK 73069. E-mail: Vincent.Wood@noaa.gov

2. APPROACH

a. Description of the numerical model

The Dowell et al. (2004) model, which adopted the method of Fiedler (1993), governed two-dimensional, axisymmetric forced convection inside a closed, impermeable cylinder that rotates at a constant angular velocity (Ω). Physically, this may be viewed as a rotating updraft that draws upon ambient vertical vorticity of 2Ω within which a tornado-like vortex develops. The governing equations in the model were solved on a uniform Cartesian grid of 50 m spacing in radial and vertical directions. The top, bottom, and lateral sides of the domain were rigid with no-slip boundary conditions.

The fields of precipitation particles contain some simplifying assumptions outlined by Dowell et al. (2004). All particles are the same size. They do not coalesce or break up and do not affect airflow. The drag coefficient is assumed to be isotropic and constant (equal to the value attained when the object is falling at its terminal fall speed in still air).

b. Doppler radar simulation

The mean Doppler velocity $\overline{V}_d$ is the volume-averaged Doppler velocity within the radar beam (e.g., Doviak and Zrnić 1993), and is given by

$$\overline{V}_d = \frac{\iiint V_d \eta \left|W_R\right|^2 f^4 dR d\theta d\phi}{\iiint \eta \left|W_R\right|^2 f^4 dR d\theta d\phi}, \quad (1)$$

where R, θ, and ϕ are in the range, azimuth, and elevation directions, respectively. The mean reflectivity factor $\overline{\eta}$ is the volume-averaged reflectivity factor within the radar beam and is expressed as

$$\overline{\eta} = \frac{\iiint \eta \left|W_R\right|^2 f^4 dR d\theta d\phi}{\iiint \left|W_R\right|^2 f^4 dR d\theta d\phi}. \quad (2)$$

The radar reflectivity factor (e.g., Battan, 1973) is calculated from

$$\eta = \sum_i n\left(D_i\right) D_i^6, \quad (3)$$

where $n\left(D_i\right)$ is the number of the i^{th} precipitation particles per unit volume and D_i is the diameter of the i^{th} particle. The range weighting function (W_R) of the radar beam is used to weight the Doppler velocity and reflectivity values at the range data point within the beam and is a trapezoidal-shaped transmitter power pulse such as the one used by the WSR-88D. The top of the trapezoid, where the weight is 1.0 has a range extent of 90 m. The base of the trapezoid, where the weight is 0.0, has a range width of 120 m. The two-way beam pattern (f^4) is the antenna pattern weighting function used to weight the reflectivity and Doppler velocity values within the effective resolution area and is given by

$$f^4 = \exp\left\{-\left[\frac{\left(\theta-\theta_o\right)^2}{2\sigma_\theta^2} + \frac{\left(\phi-\phi_o\right)^2}{2\sigma_\phi^2}\right]\right\}, \quad (4)$$

where the standard deviations of the Gaussian density, $\sigma_\theta^2\left[=\theta_e^2/\left(16\ln 2\right)\right]$ and $\sigma_\phi^2\left[=\phi_3^2/\left(16\ln 2\right)\right]$, are related to the half-power (-3 dB) beamwidth, and θ_e is the horizontal (effective) half-power beamwidth, and ϕ_3 is the vertical half-power beamwidth. Eq. (4) is a simple Gaussian function that neglects the effects of antenna sidelobes.

In Eq. (1), V_d is calculated explicitly from the 3-D motion fields of precipitation particles (not air motion) within the beam and is given by

$$V_d = u_p \sin\gamma\cos\phi + \upsilon_p \cos\gamma\cos\phi + \left(w_p + w_t\right)\sin\phi, \quad (5)$$

where u_p, υ_p, and w_p are, respectively, the radial, tangential and vertical components of precipitation motion. The term w_t is the terminal fall velocity of a precipitation particle. The geometry for computing Eq. (5) is shown in Fig. 1.

The analytical simulation of a WSR-88D was used to generate simulated Doppler velocity measurements by scanning across the tornado-like vortex. Simulation of the radar sampling did not follow that of an actual radar. Instead of averaging radar pulses to produce a simulated mean Doppler velocity (radar reflectivity) value, mean Doppler velocity (radar reflectivity) was obtained by averaging the reflectivity-weighted Doppler velocity components (reflectivities) within the effective resolution volume of the radar beam, as shown from Eq. (1) [Eq. (2)].

Effective beamwidth is a broadened version of the antenna pattern beamwidth that arises owing to antenna rotation during the time it takes to collect the required number of samples (Doviak and Zrnić 1993, pp. 193-197). Effective beamwidth is a linear function of three radar parameters: antenna rotation rate, number of pulses transmitted and received, and time interval between pulses. The effective beamwidth can be reduced by decreasing one or more of the three parameters.

In this study, we use the same 1.0° azimuthal sampling interval used by WSR-88Ds. However, we also use 0.5° azimuthal sampling interval to show how this finer

resolution data can better resolve measurements within a tornado (e.g., Brown et al. 2002; Brown et al. 2004). Fine-resolution data are achieved by sampling half the number of pulses that are used for 1.0^o resolution, while keeping the antenna rotation rate constant. The average half-power beamwidth of WSR-88Ds is 0.89^o (Brown et al. 2002). Thus, azimuthal resolutions of 0.5^o and 1.0^o produce effective beamwidths of 1.02^o and 1.39^o, respectively, based on Fig. 1 of Brown et al. (2002), and will be used in this study.

3. NUMERICAL MODELING RESULTS

By varying the model domain's rotation rate and the size and strength of the region of positive buoyancy, one can simulate vortices of various sizes, intensities, and types (one celled and two celled) in the Dowell et al. (2004) model. Dowell et al. also used object motions that ranged in size from small raindrops to bricks and sheets of plywood.

We conducted two experiments to investigate the centrifugal effects of raindrops on radial distributions of reflectivity within tornadoes. In EXP I, all the raindrops were 0.5 mm in diameter (terminal fall velocity, w_t, of -2 m s^{-1}) and in EXP II were 1.3 mm in diameter (w_t = -5 m s^{-1}). Terminal fall velocities (based on Gunn and Kinzer (1949) measurements) were assumed to be constant with height.

The simulation was initialized with solid-body rotation Ω of 10^{-2} s^{-1}, and the CAPE at the center of the domain was 3300 J kg^{-1}. The simulation produced a rather broad tornado-like vortex having an average core diameter of 0.75 km. Vertical cross-sections of the radial, tangential, and vertical velocity components of airflow in the tornado-like vortex at t = 600 s are shown in Figs. 2-4. Since radial and vertical velocities were zero at t = 0, radial inflow in the surface boundary layer was generated when the radial pressure gradient acted to drive the airflow near the surface toward the vertical axis at t > 0 (Fig. 2). The resulting radial velocity produced a strong updraft near the axis (Fig. 4). Tangential velocity maximum was noticeable near the surface and r = 0 (Fig. 3).

Figure 5 reveals reflectivity structures of the tornado region for EXPs I and II. For EXP I, the 0.5-mm diameter raindrops are lifted by the updraft, slightly ejected from the tornado core, and accumulated outside the core (Figs. 5a and 6a). For EXP II of the 1.3-mm diameter raindrops, there are two reflectivity maxima: one greater than 25 dBZ outside the radius of the tornado's maximum tangential airflow and the other one greater than 30 dBZ at low-altitudes and inside the radius of tangential velocity peak (Fig. 5b). The streamlines (Fig. 6b) show that reflectivity maximum results mainly from concentration of the 1.3-mm diameter raindrops just inside the core radius of maximum tangential wind near the surface. The concentrated raindrops then are lifted by the updraft, while they simultaneously are centrifuged outward. Some raindrops are carried downward by the downdraft outside the core radius of maximum tangential wind, before re-entering into the strong inflow layer at low-altitudes. Consequently, a surrounding annulus of relatively high number concentration slightly expands with height (Fig. 5b). Recycling of 1.3-mm diameter raindrops by the near-surface inflow and updraft is more pronounced than that of 0.5-mm diameter raindrops, as shown in the streamlines of Fig. 6.

In the subsequent sections, we explore how the centrifuging of raindrops directly impacts simulated Doppler radar reflectivity measurements.

4. DOPPLER RADAR SIMULATIONS

Doppler velocity and reflectivity measurements from WSR-88D radars provide important input to forecasters as they prepare to issue short-term tornado warnings. Currently, WSR-88D *collect* full-resolution base data (reflectivity, Doppler velocity, and spectrum width) with an azimuthal spacing of 1.0^o and range spacing of 0.25 km. Doppler velocity and spectrum width are *recorded and displayed* at this spacing. Full-resolution reflectivity measure-ments are averaged over four range intervals and are *recorded and displayed* at coarser 1.0 km intervals.

Brown et al. (2004) compared displays of current-resolution WSR-88D Doppler velocity and reflectivity signatures in severe storms with displays showing finer-resolution

signatures obtained by a test-bed WSR-88D. Fine-resolution data were produced by processing data at 0.5° azimuthal intervals rather than at conventional 1.0° intervals and by using range data at 0.25 km intervals for reflectivity. As a consequence, fine-resolution displays have twice the number of Doppler velocity and spectrum width data points and eight times the number of reflectivity data points. Severe storm characteristics (such as bounded weak echo regions, hook echo regions, tornadic vortex signatures, etc.) are more clearly depicted with finer-resolution data.

We now consider Doppler radar sampling issues associated with differential weighting by the nonuniform reflectivity distribution across the tornado vortex. Figure 7 shows simulated radar reflectivity signatures that correspond to the annulus of high reflectivity surrounding a low-reflectivity eye. The signatures are located 40 km north of the radar and at elevation angle of 0.5°. It is assumed that the tornado is centered midway between two azimuthal bins at the same range (e.g., Wood and Brown 1997). Radar reflectivities are shown in the figures for two effective beamwidths and associated azimuthal and range sampling intervals. The effective half-power beam-widths of 1.39° and 1.02° at 40 km from the radar are, respectively, 0.97 and 0.71 km. Coarser- and finer-resolution signatures are considered for comparison purposes. A small "knob" of high radar reflectivities, shown with coarser-resolution data (in the left panel of Fig. 7), is caused by two factors. The first factor is owing to the smearing effect of the radar beam. The second factor is the average of full-resolution reflectivity measurements over four range intervals of 0.25 km so that the measurements are recorded and displayed at coarser 1.0 km intervals.

Minimum radar reflectivities surrounded by the annulus of slightly maximum radar reflectivities are clearly depicted with finer-resolution data, as seen in the right panel of Fig. 7. The diameter of the annulus is about 1 km. This effect is attributed to the weak centrifuging of the 0.5-mm diameter raindrops by the vortex. The weak annulus is produced using a smaller effective beamwidth and associated smaller azimuthal and range sampling intervals because (a) the effective beamwidth resulting from 0.5° azimuthal sampling interval is narrower than that for 1.0° azimuthal sampling interval, and (b) with four times the number of reflectivity data points in the range direction, there is better sampling of the smaller-scale radar reflectivities.

Figure 8 presents the simulated radar reflectivity signatures which correspond to EXP II in Fig. 5b. A prominent "knob" of high reflectivities is clearly depicted in Fig. 8. High reflectivities in the knob are similar in appearance to the 0.5° KTLX WSR-88D observations of "knob" reflectivities at proximity to the radar during the 3 May 1999 Oklahoma City tornado (Burgess et al. 2002). The "knob" reflectivities in Fig. 8 are produced by maximum reflectivities due to recycling of the 1.5-mm raindrops by the vortex at low levels (Figs. 5b and 6b). The stronger "knob" reflectivities in the right panel of Fig. 8 are produced because of the advantage of employing a smaller effective beamwidth and associated smaller azimuthal and range sampling intervals to better sample small-scale reflectivities.

In the examples shown thus far, simulated WSR-88D measurements have been computed at 40 km from the radar and at elevation angle of 0.5°. We now consider a different range and elevation angle. The 20-km range and 6.2° elevation angle are chosen. The effective half-power beam-widths of 1.39° and 1.02° at this range are, respectively, 0.49 and 0.36 km.

Figures 9 and 10 reveal interesting features in the simulated radar reflectivity measurements. Radar reflectivity minimum occurs within an annulus of high radar reflectivities, which corresponds to the modeled reflectivity structures at the height of 2.20 km (Fig. 5). In EXP II, the narrow reflectivity annulus surrounding the tornado at this altitude is located 0.73 km from the vortex axis, which is slightly farther away than the annulus in EXP I (Fig. 5). This effect is attributed to strong centrifuging of the 1.3-mm diameter raindrops by the vortex. The distinct overall improvement of radar reflectivity signatures using the smaller effective beamwidth and the smaller azimuthal and range sampling intervals is evident (right panels of Figs. 9 and 10).

5. SUMMARY

Simulated radar reflectivity measurements of a tornado having a weak reflectivity center were presented using coarser- and finer-resolution data. At lowest elevation angle, a "knob" radar reflectivity signature is produced when recycling of small-medium (1.5-mm diameter) raindrops by the vortex results in reflectivity maximum in a surrounding annulus inside the radius of precipitation tangential motion peak. The eye of radar reflectivities is produced at a high elevation angle when 0.5-mm and 1.5-mm diameter raindrops are lifted by the tornado's updraft, ejected from the tornado core, and accumulated outside the core.

Although we have limited this study to simulated radar reflectivities only, we will continue investigating the effect of centrifuging of raindrops directly impact simulated WSR-88D measurements (Doppler velocities and radar reflectivities) at different ranges and elevation angles.

6. REFERENCES

Battan, L. J., 1973: *Radar Observation of the Atmosphere*. University of Chicago Press, 324 pp.

Bluestein, H. B., and A. L. Pazmany, 2000: Observations of tornadoes and other convective phenomena with a mobile 3-mm wavelength, Doppler radar: The spring 1999 field experiment. *Bull. Amer. Meteor. Soc.,* **131,** 2968-2984.

Brown, R. A., 1998: Nomogram for aiding the interpretation of tornadic vortex signatures measured by Doppler radar. *Wea. Forecasting,* **13,** 505-512.

_____, and L. R. Lemon, 1976: Single Doppler radar vortex recognition: Part II-Tornadic vortex signatures. Preprints*, 17th Conf. on Radar Meteorology,* Seattle, WA, Amer. Meteor. Soc., 104-109.

_____, _____, and D. W. Burgess, 1978: Tornado detection by pulsed Doppler radar. *Mon. Wea. Rev.,* **106,** 29-38.

_____, V. T. Wood, and D. Sirmans, 2002: Improved tornado detection using simulated and actual WSR-88D data with enhanced resolution. *J. Atmos. Oceanic Technol.,* **19,** 1759-1771.

_____, B. A. Flickinger, E. Forren, D. M. Schultz, D. Sirmans, P. L. Spencer, V. T. Wood, and C. L. Ziegler, 2004. Improved detection of severe storms using experimental fine-resolution WSR-88D measurements. *Wea. Forecasting* (in press).

Burgess, D. W., M. A. Magsig, J. Wurman, D. C. Dowell, and Y. Richardson, 2002: Radar observations of the 3 May 1999 Oklahoma City tornado. *Wea. Forecasting,* **17,** 456-471.

Dowell, D. C., C. R. Alexander, J. M. Wurman, and L. J. Wicker, 2004: Centrifuging of hydrometeors and debris in tornadoes: Radar-reflectivity patterns and wind-measurements errors. *Mon. Wea. Rev.,* **132,** (accepted).

Doviak, R. J., and D. S. Zrnić, 1993: *Doppler Radar and Weather Observations.* 2nd, ed., Academic Press, 562 pp.

Fielder, B. H., 1993: Numerical simulation of axisymmetric tornadogenesis in forced convection. *The Tornado: Its Structure, Dynamics, Prediction, and Hazards.* Geophys. Monogr. No. 79, Amer. Geophys. Union, 41-48.

Gunn, R., and G. D. Kinzer, 1949: The terminal velocity of fall for water droplets in stagnant air. *J. Meteor.*, **6,** 243-248.

Rankine, W. J. M., 1901: *A Manual of Applied Mechanics.* 16th ed. Charles Griff and Co., 680 pp.

Snow, J. T., 1984: On the formation of particle sheaths in columnar vortices. *J. Atmos. Sci.,* **41,** 2477-2491.

Wakimoto, R. M., and B. E. Martner, 1992: Observations of a Colorado tornado. Part II: Combined photogrammetric and Doppler radar analysis. *Mon. Wea. Rev.,* **120,** 522-543.

Wood, V. T., and R. A. Brown, 1997: Effects of radar sampling on single-Doppler velocity signatures of mesocyclones and tornadoes. *Wea. Forecasting,* **12,** 929-939.

Wurman, J., 2002: The multiple-vortex structure of a tornado. *Wea. Forecasting,* **17,** 473-505.

_____, and S. Gill, 2000: Finescale radar observations of the Dimmitt, Texas (2 June 1995), tornado. *Mon. Wea. Rev.,* **128,** 2135-2164.

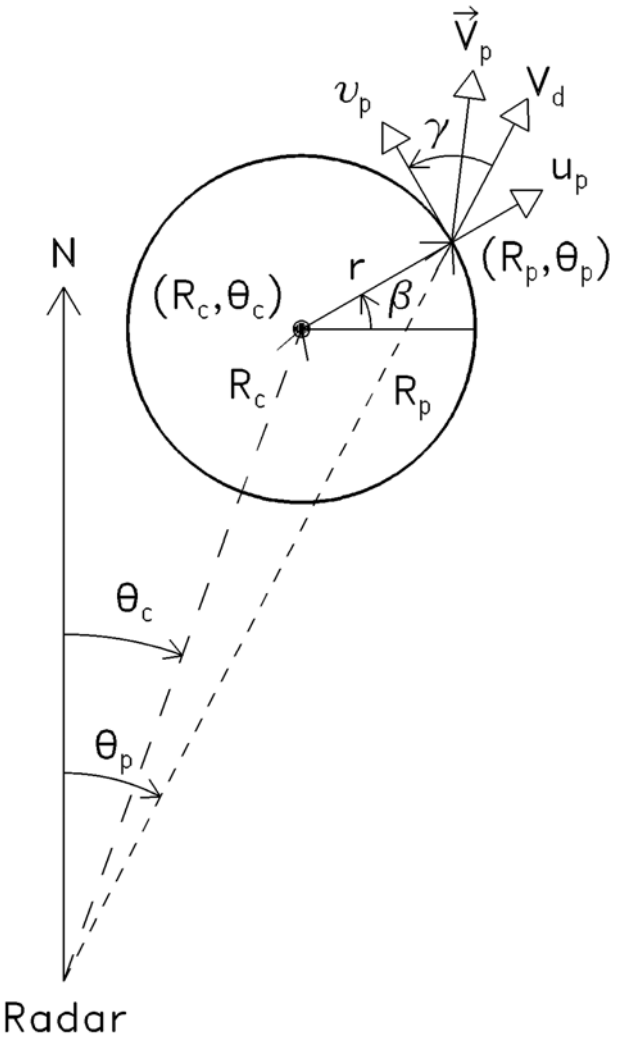

Fig. 1. Geometry for computing Doppler velocity V_d at a point (R_p,θ_p) relative to a true tornado center (R_c,θ_c). u_p and υ_p, respectively, are radial and tangential velocity components of a precipitation particle located at the radius (r) from the vortex center. $\vec{V}_p$ is a 2-D motion vector of the particle. β is the angle (positive in a counterclockwise direction) between east and the radial direction from the vortex center. $\gamma\ (=\beta+\theta_p)$ is the angle between the radar viewing direction (θ_p) at a point (R_p,θ_p) and the tangential velocity component (υ_p).

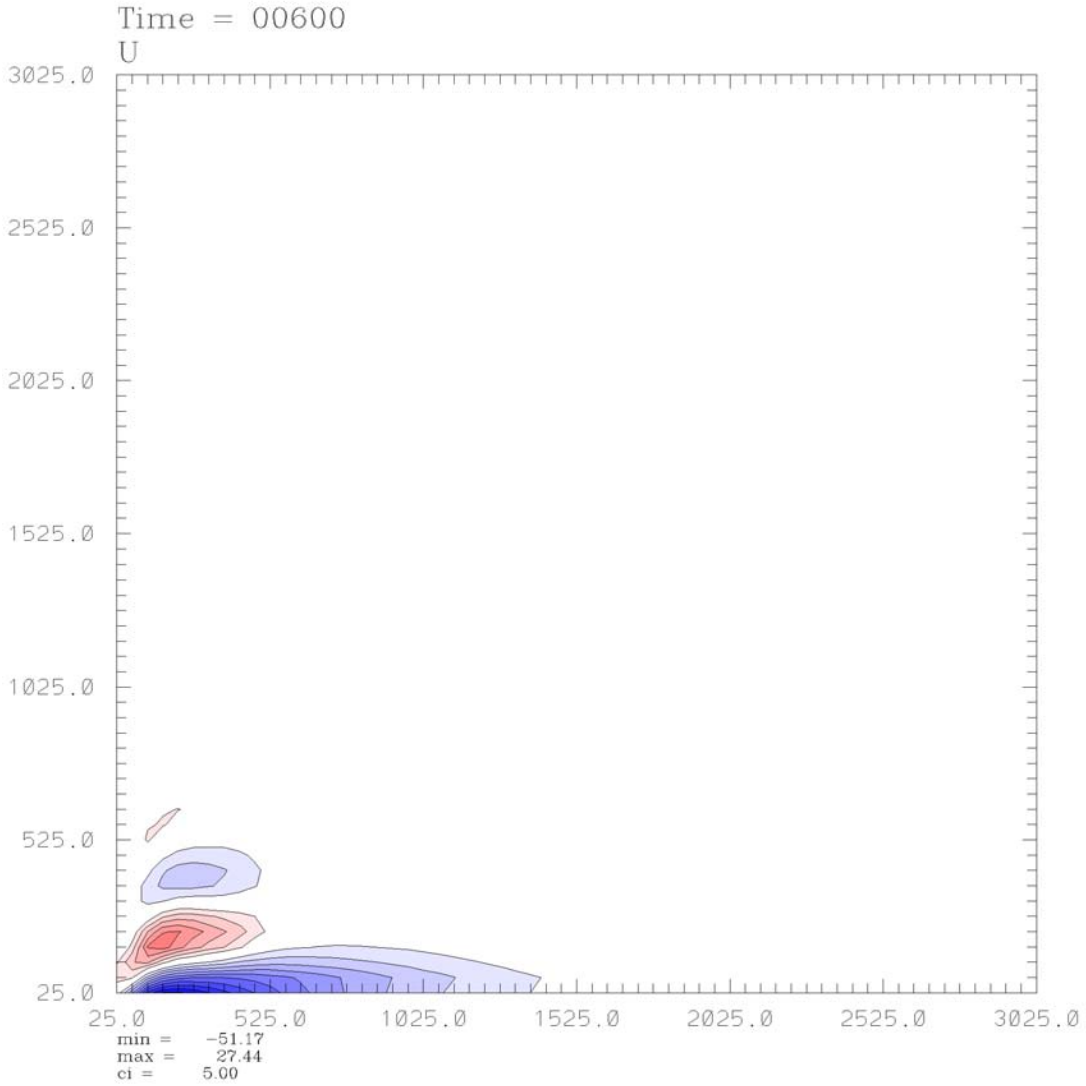

Fig. 2. Plot of airflow radial velocity (u_a) in the r-z plane for the simulated tornado at *t* = 600 s. Heights and radial distances are in meters. Red (blue) contours represent positive (negative) values, excluding zero contours. Contour interval is 5 m s^{-1}. Maximum inflow is -51.2 m s^{-1} and maximum outflow is 27.4 m s^{-1}.

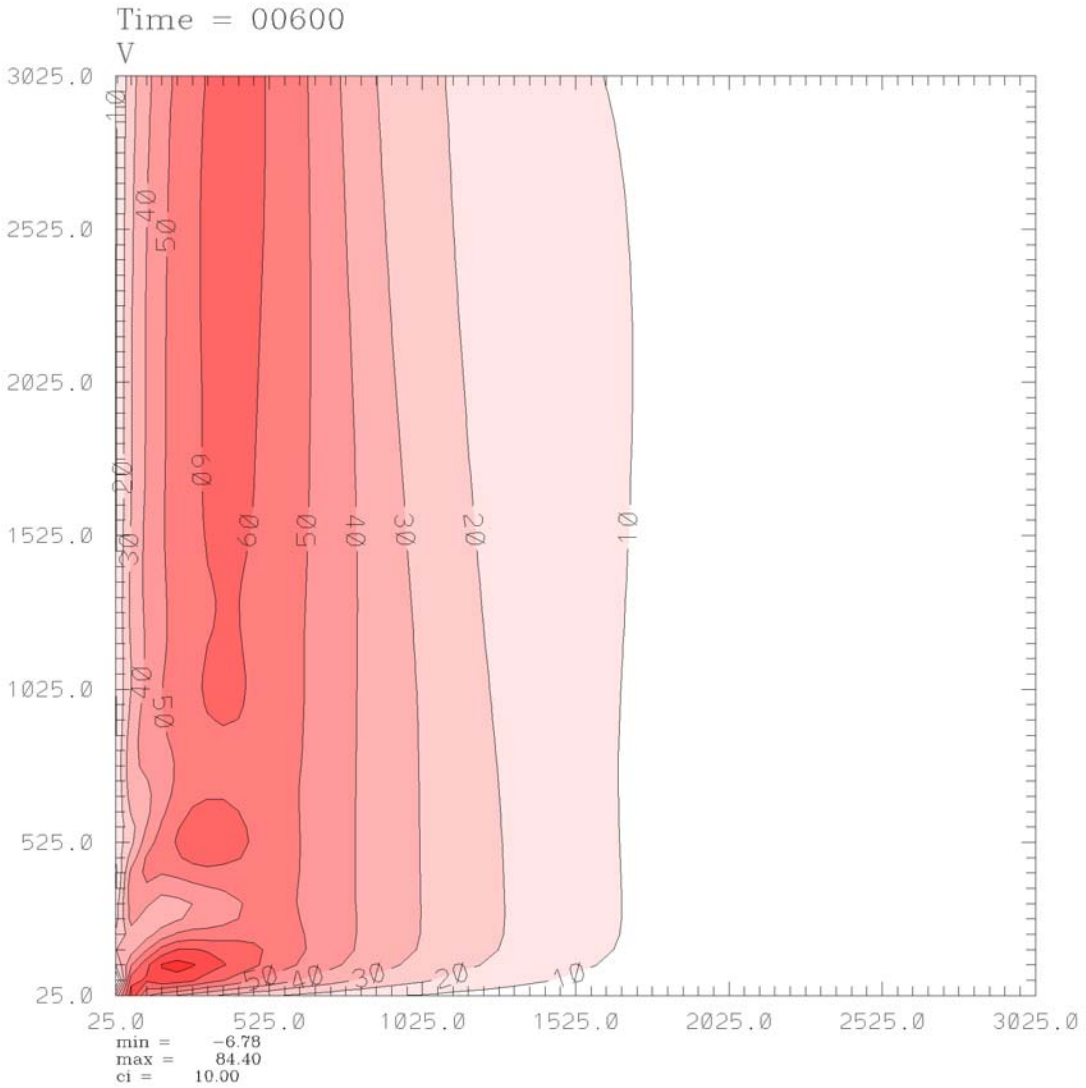

Fig. 3. Same as Fig. 2, except for airflow tangential velocity (υ_a). Contour interval is 10 m s^{-1} and the maximum value is 84.4 m s^{-1}.

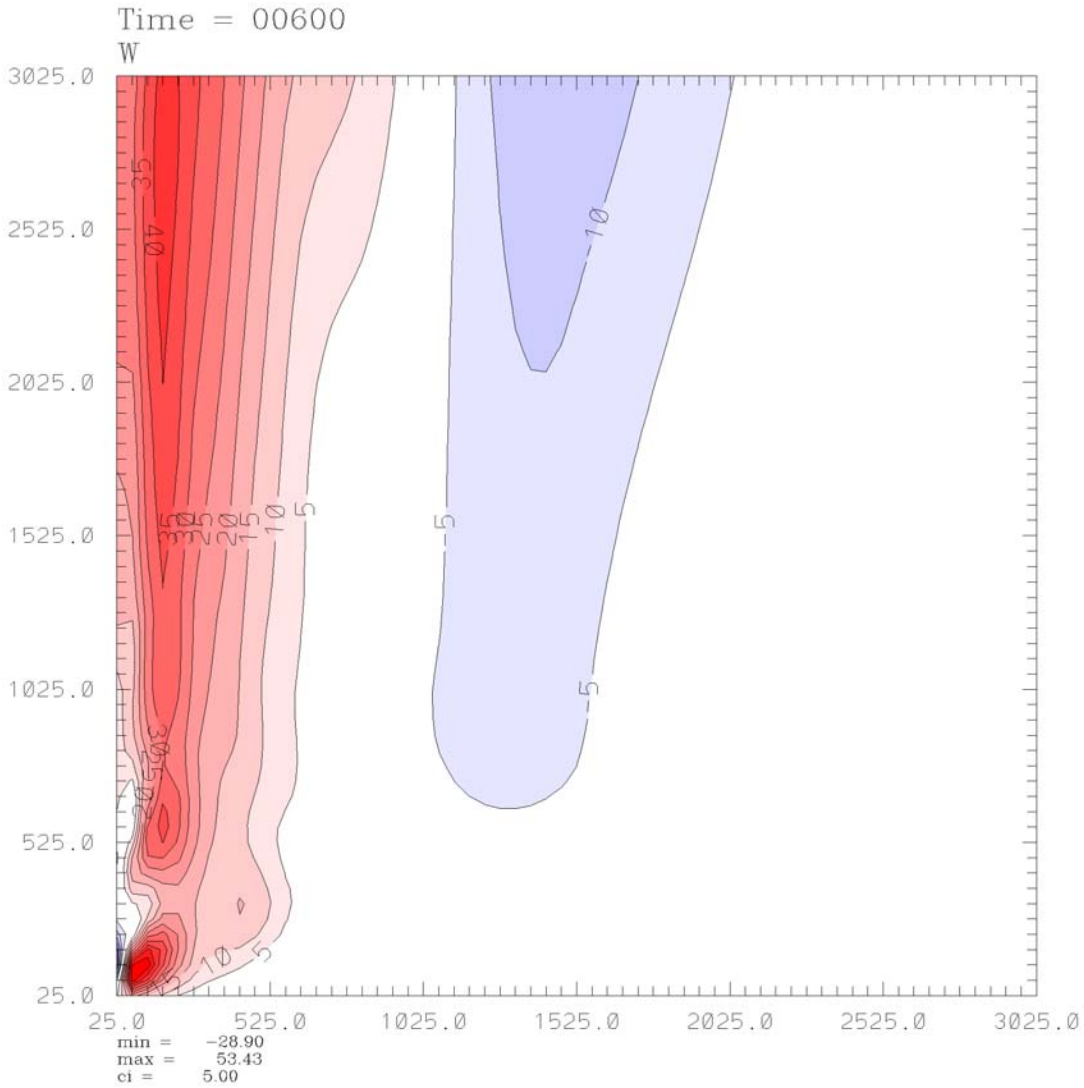

Fig. 4. Same as Fig. 2, except for airflow vertical velocity (w_a). Contour interval is 5 m s^{-1}. Maximum updraft value is 53.4 m s^{-1} and maximum downdraft value is -28.9 m s^{-1} (on the axis near the ground).

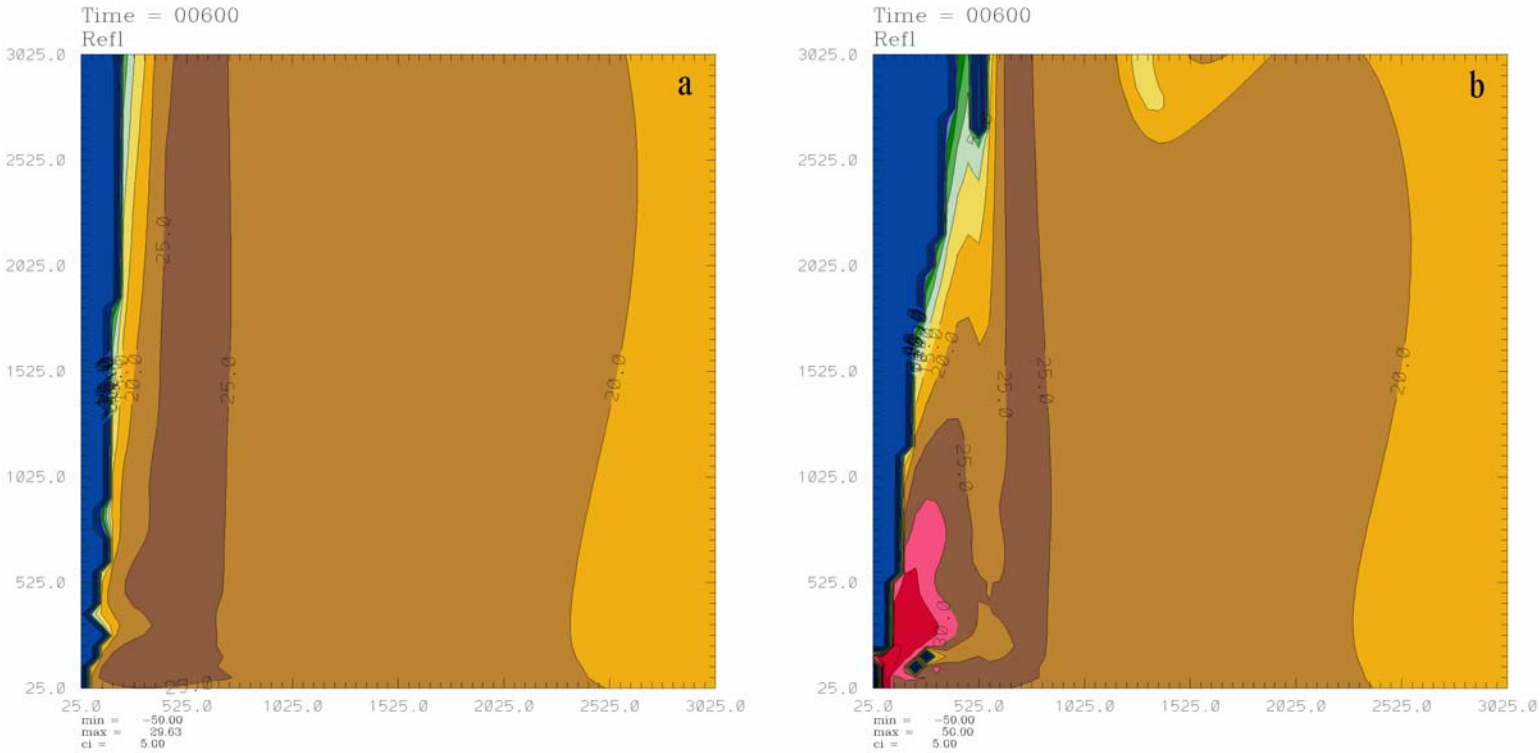

Fig. 5. Comparison of reflectivity (dBZ) for (a) EXP I of 0.5-mm diameter raindrops and (b) EXP II of 1.3-mm diameter raindrops at t = 600 s. Heights and radial distances are in meters. Contour interval is 5 dBZ and the contour value on the right side of each panel is 20 dBZ. Maximum value in (a) is 29.6 dBZ and in (b) is 50.0 dBZ.

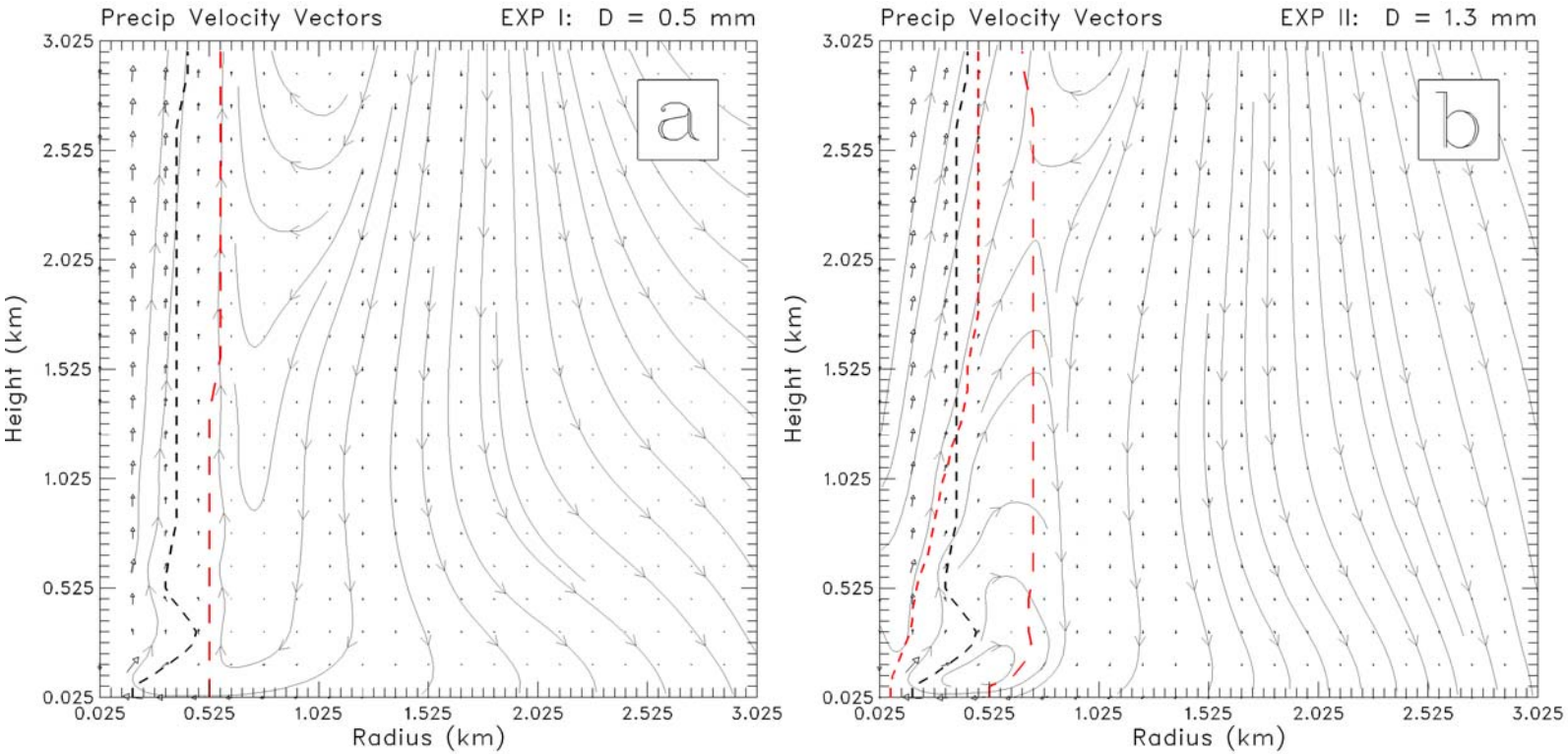

Fig. 6. Precipitation particle motion vectors with superimposed precipitation streamlines for (a) EXP I of 0.5-mm diameter raindrops and (b) EXP II of 1.3-mm diameter raindrops in the r-z plane at t = 600 s. Black dashes represent the vortex's core radius of maximum tangential airflow. Red short and long dashes represent the modeled reflectivity's core radii of maximum reflectivity.

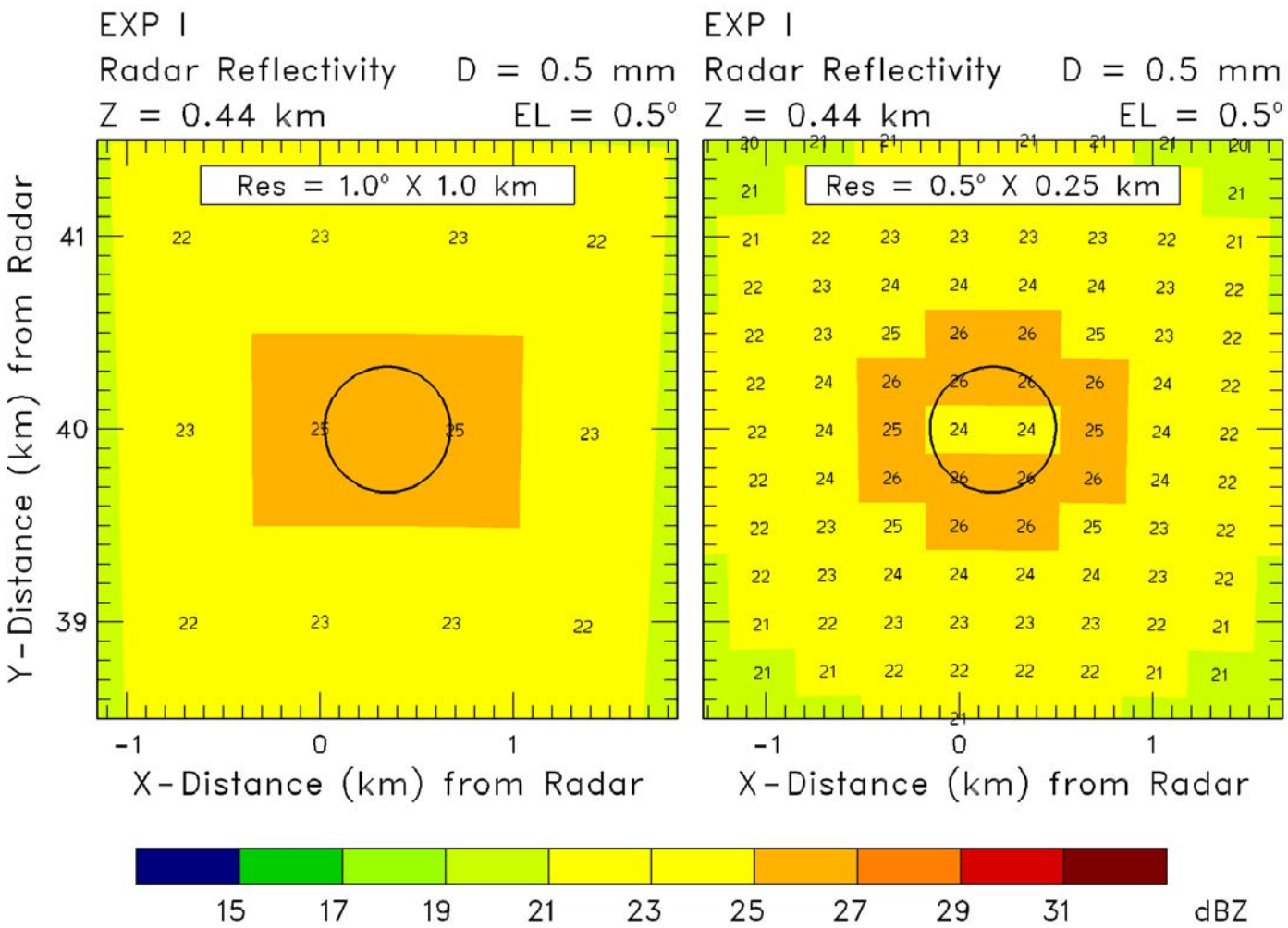

Fig. 7. Plan views of simulated radar reflectivity signatures measured at elevation angle of 0.5° by a Doppler radar located 40 km from a modeled tornado vortex centered at the black circle for EXP I of 0.5-mm diameter (D) raindrops. Black circle represents the circle of airflow tangential velocity maximum. Height (Z) and elevation angle (EL) are indicated at the top of each panel. The radar is located beyond the bottom of the figure. Border tick marks are 0.1 km apart. The vortex center is located midway between two azimuthal locations. The color horizontal bar represents the radar reflectivity scale (dBZ), as indicated at the bottom. The size of each panel is 3x3 km.

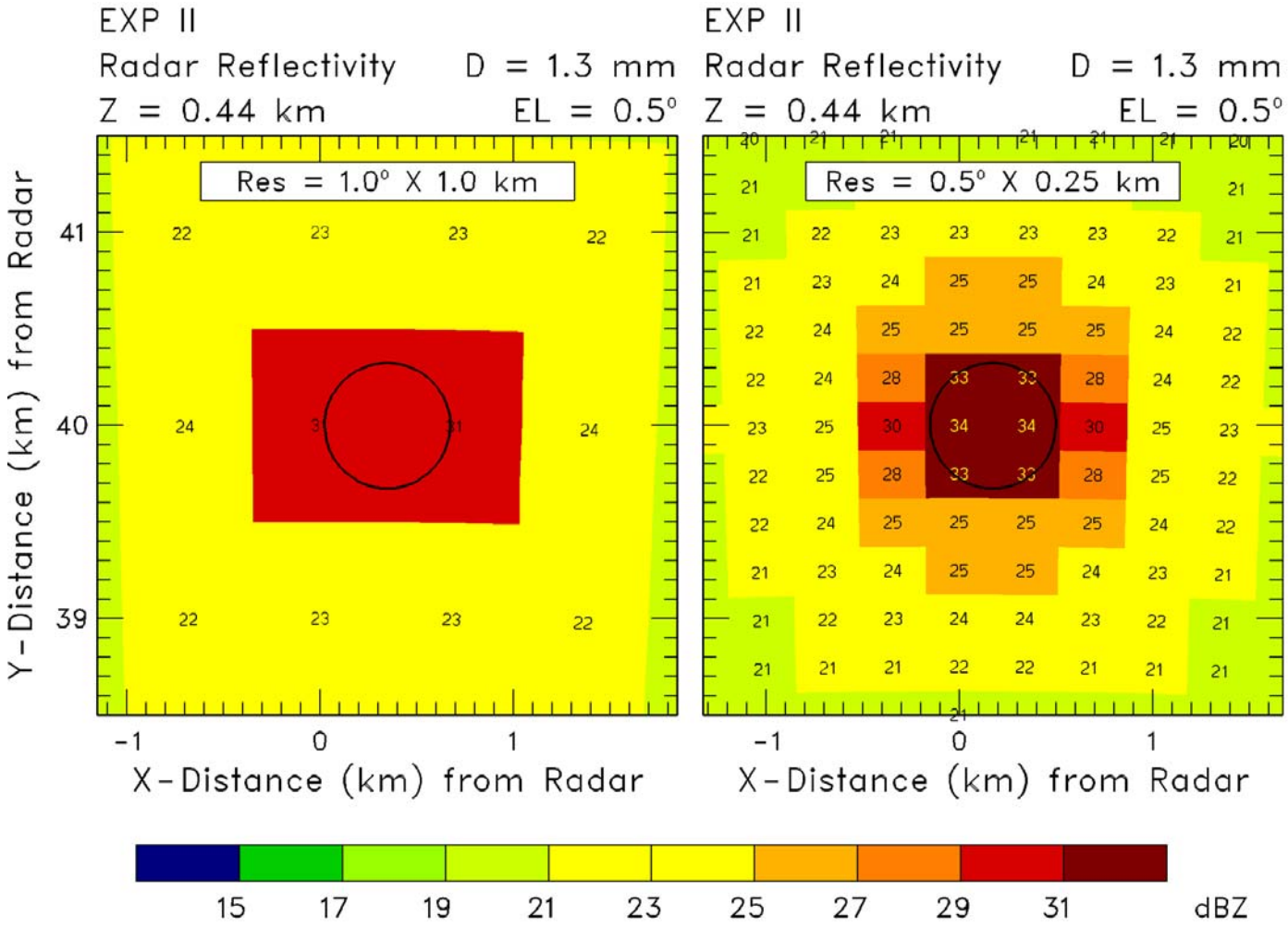

Fig. 8. Same as Fig. 7, except for EXP II of 1.3-mm diameter raindrops.

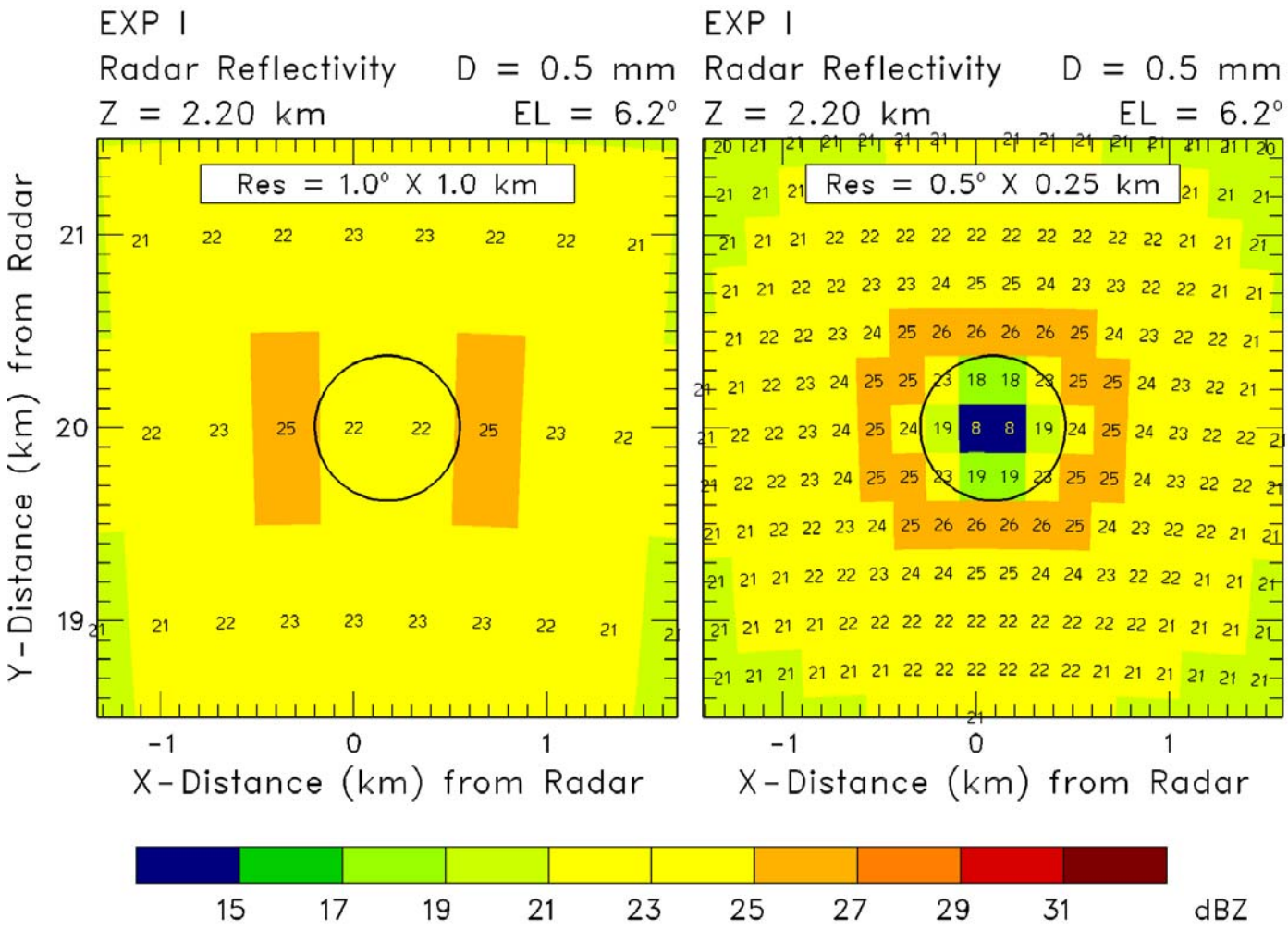

Fig. 9. Same as Fig. 7, except at a 20-km range from the radar and at elevation angle of 6.2°.

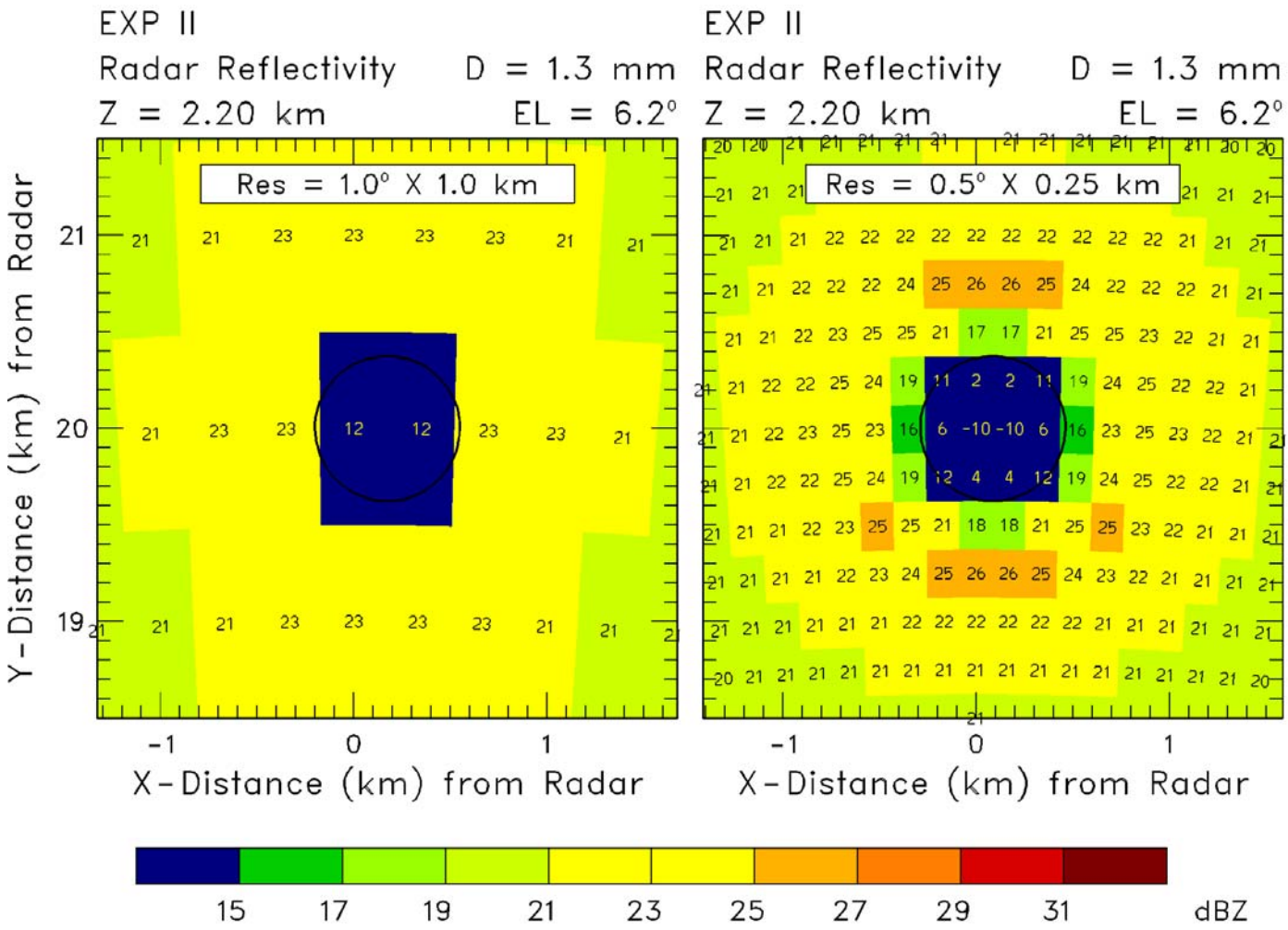

Fig. 10. Same as Fig. 9, except for EXP II of 1.3-mm diameter raindrops.